AGU PUBLICATIONS

JGR

Journal of Geophysical Research: Oceans

RESEARCH ARTICLE

10.1002/2014JC010407

**Key Points:**
- Ocean and biological responses to strong-wind events were observed in the Arctic
- Wind-induced ocean mixing and inertial motion impact primary production
- Subsurface silicate maximum plays an important role in diatom production

**Correspondence to:**
S. Nishino,
nishinos@jamstec.go.jp

**Citation:**
Nishino, S., Y. Kawaguchi, J. Inoue, T. Hirawake, A. Fujiwara, R. Futsuki, J. Onodera, and M. Aoyama (2015), Nutrient supply and biological response to wind-induced mixing, inertial motion, internal waves, and currents in the northern Chukchi Sea, *J. Geophys. Res. Oceans*, *120*, 1975–1992, doi:10.1002/2014JC010407.

Received 28 AUG 2014
Accepted 12 FEB 2015
Accepted article online 18 FEB 2015
Published online 26 MAR 2015
Corrected 8 MAY 2015



# Nutrient supply and biological response to wind-induced mixing, inertial motion, internal waves, and currents in the northern Chukchi Sea

**Shigeto Nishino[1], Yusuke Kawaguchi[1,2], Jun Inoue[1,3], Toru Hirawake[4], Amane Fujiwara[3,4], Ryosuke Futsuki[5], Jonaotaro Onodera[1], and Michio Aoyama[1,6]**

[1]Research and Development Center for Global Change, Japan Agency for Marine-Earth Science and Technology, Yokosuka, Japan, [2]Polar Science Center, Applied Physics Laboratory, University of Washington, Seattle, Washington, USA, [3]National Institute of Polar Research, Tachikawa, Japan, [4]Faculty of Fisheries Sciences, Hokkaido University, Hakodate, Japan, [5]Graduate School of Fisheries Sciences, Hokkaido University, Hakodate, Japan, [6]Institute of Environmental Radioactivity, Fukushima University, Fukushima, Japan

**Abstract** A fixed-point observation station was set up in the northern Chukchi Sea during autumn 2013, and for about 2 weeks conductivity-temperature-depth (CTD)/water samplings (6 h) and microstructure turbulence measurements (2 to 3 times a day) were performed. This enabled us to estimate vertical nutrient fluxes and the impact of different types of turbulent mixing on biological activity. There have been no such fixed-point observations in this region, where incoming low-salinity water from the Pacific Ocean, river water, and sea-ice meltwater promote a strong pycnocline (halocline) that stabilizes the water column. Previous studies have suggested that because of the strong pycnocline, wind-induced ocean mixing could not change the stratification to impact biological activity. However, the present study indicates that a combined effect of an uplifted pycnocline accompanied by wind-induced inertial motion and turbulent mixing caused by intense gale-force winds ($>10$ m s$^{-1}$) did result in increases in upward nutrient fluxes, primary productivity, and phytoplankton biomass, particularly large phytoplankton such as diatoms. Convective mixing associated with internal waves around the pycnocline also increased the upward nutrient fluxes and might have an impact on biological activity there. For diatom production at the fixed-point observation station, it was essential that silicate was supplied from a subsurface silicate maximum, a new feature that we identified during autumn in the northern Chukchi Sea. Water mass distributions obtained from wide-area observations suggest that the subsurface silicate maximum water was possibly derived from the ventilated halocline in the Canada Basin.

## 1. Introduction

In recent decades, the Arctic has rapidly lost its summer sea-ice cover [*Stroeve et al*., 2007; *Comiso et al*., 2008; *Kwok et al*., 2009], which may significantly amplify upper ocean responses to atmospheric forcing that are associated with sea-ice formation/melting, ocean stratification and mixing, seawater nutrient distributions, and marine biological activity [*Rainville et al*., 2011]. Furthermore, there has been a general increase in the frequency and intensity of cyclones in the Arctic and a northward shift in storm tracks during summer and in other seasons [e.g., *Orlanski*, 1998; *Serreze et al*., 2000; *McCabe et al*., 2001; *Zhang et al*., 2004; *Sepp and Jaagus*, 2011]. Local storms in ice-free regions of the Arctic Ocean may generate profound inertial motion in the upper water and enhance interior mixing, causing turbulent energy levels to increase to levels comparable to those in lower latitude seas [*Rainville and Woodgate*, 2009]. In such seas, field studies of the passage of typhoons have suggested that ecosystem responses start with episodic nutrient loading, followed by sizable diatom blooms, intense grazing pressure, and a significant carbon flux [*Chang et al*., 1996; *Hung and Gong*, 2011; *Chung et al*., 2012; *Tsuchiya et al*., 2013].

However, in the Pacific sector of the Arctic Ocean (Pacific Arctic), inflows of low-salinity water from the Pacific Ocean and rivers promote a strong pycnocline (halocline) that stabilizes the water column, and the sea-ice melt enhances stratification during summer [*Yamamoto-Kawai et al*., 2005; *Carmack and Wassmann*, 2006]. Thus, in the Pacific Arctic, vertical mixing accompanying upward nutrient supply during the passage

of a storm has been considered insignificant in primary productivity [*Carmack and Wassmann*, 2006]. A field study conducted at a fixed overwintering site in the southeast Beaufort Sea suggested that wind-driven mixing could not increase nutrient concentrations in the surface layer in autumn because of the presence of a strong pycnocline, despite the episodic passage of storms over the area [*Tremblay et al*., 2008]. Furthermore, winter convection or brine rejection could not replenish the surface nutrients in the region. Conversely, *Zhang et al*. [2014] used a coupled biophysical model to indicate that a great Arctic summer cyclone enhanced primary productivity on the Pacific Arctic shelves, where nutrient availability was increased by intensified mixing. However, compared to the clear responses to typhoon events in lower latitude seas, to date, there is no observational evidence of an increase in nutrient availability and an ensuing increase in primary productivity during storm events in the Pacific Arctic.

The most straightforward way to understand ocean and biological responses to atmospheric events such as strong winds is an Eulerian approach, i.e., a fixed-point observation (FPO), as conducted by *Tremblay et al*. [2008]. Although their approach provided various new findings, including the results mentioned above regarding the association of vertical stability and nutrient dynamics with atmospheric forcing, the frequency of nutrient observations was very limited (every third to sixth day), making it difficult to detect daily and diurnal variability. As a result, the temporal variation in nutrient distributions related to physical processes such as inertial motion and internal waves generated by winds, and their associated vertical mixing, has not been fully investigated. A survey with high temporal resolution (i.e., resolving inertial motion and internal waves) is required to capture various mixing processes and their effects on stratification, nutrient distribution, and biological activity. Furthermore, the actual fluxes of nutrients are seldom quantified and compared to concurrent biological processes. Thus, multidisciplinary observations are indispensable (i.e., surface meteorological conditions; physical and chemical water properties; turbulent mixing of heat, salt, and nutrients; and indices of biological activities such as chlorophyll *a* and primary productivity). To date, no such study has been conducted at an FPO station in the Pacific Arctic.

We established an FPO station in the northern Chukchi Sea (72.75°N, 168.25°W; see Figure 1), where the water column consisted of two layers separated by a pycnocline: a warmer/fresher/nutrient-poor upper layer and a colder/saltier/nutrient-rich lower layer [*Coachman et al*., 1975; *Walsh et al*., 1989; *Weingartner et al*., 2005]. In general, stratification is weaker in the Chukchi Sea than on other Pacific Arctic shelves because the surface salinity is higher due to less influence of river waters [*Aagaard and Carmack*, 1989]; therefore, the ocean may be sensitive to wind forcing and wind-driven mixing may occur more easily. The FPO station is far from the main pathways of Pacific-origin water [*Weingartner et al*., 2005]; hence, we can assume a minimal influence from horizontal intrusions of different water masses. The station is also located away from a plume of high nutrient concentrations via the Bering Strait [*Springer and McRoy*, 1993], but primary productivity around the station in the northern Chukchi Sea is comparable to, or more likely higher than, that in the central Chukchi Sea [*Hill and Cota*, 2005]. From the perspective of biological activity, the northern Chukchi Sea is a key area, but the mechanisms that maintain the high productivity there are not well understood.

We remained at the FPO station in the northern Chukchi Sea for about 2 weeks during autumn 2013, performed a hydrographic survey with high temporal resolution (conductivity-temperature-depth (CTD)/water sampling every 6 h), and took microstructure turbulence measurements that enabled us to estimate the vertical nutrient fluxes and the impact of different types of turbulent mixing on biological activity. In addition to the FPO, we conducted wide-area observations from the Chukchi Sea to the Canada Basin to determine water mass distributions and their effects on the water column at the FPO station. Using the FPO station data, we investigated ocean and biological responses to atmospheric events such as strong winds during autumn in the northern Chukchi Sea. Furthermore, we analyzed the mechanism by which biological activity, such as diatom production, was maintained at the FPO station in terms of the shelf-basin interaction of water masses, deduced from the wide-area observations.

## 2. Data and Methods

### 2.1. R/V Mirai Arctic Cruise 2013

We conducted meteorological and hydrographic surveys from late summer to autumn 2013 (28 August to 7 October) over the Chukchi Sea and the Canada Basin (Figure 1), onboard the R/V Mirai of the Japan Agency

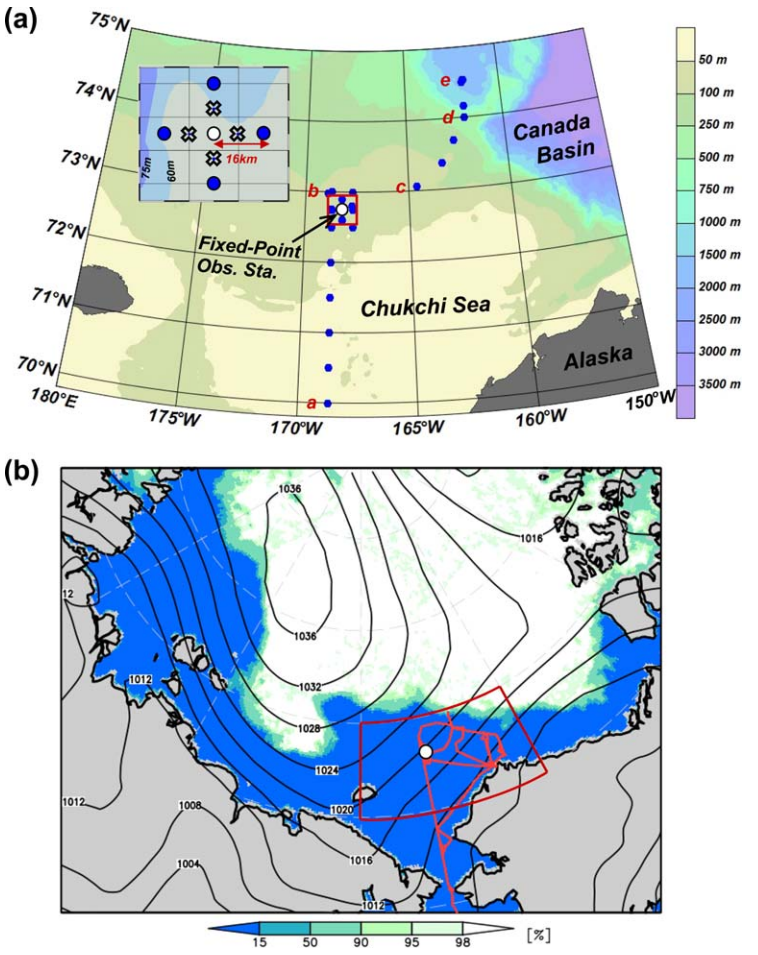


**Figure 1.** (a) Map showing the bathymetric features of the study area and locations of the hydrographic stations of the R/V Mirai cruise in 2013 (dots). The white dot at 72.75°N, 168.25°W represents a fixed-point observation (FPO) station during the period 10–26 September 2013. Along lines connecting the positions a, b, c, d, and e on the map, we plotted vertical sections from the Chukchi shelf to the Canada Basin in Figure 10. The embedded map on the upper left is an enlarged view of around the FPO station indicated by the red square. The white dot at the center of the embedded map is the FPO station, which was encompassed by CTD (blue dots) and XCTD (crosses) stations. (b) Sea-ice concentrations (%) derived from the AMSR2 on 20 September 2013. Contours indicate the sea level pressure (hPa) of ERA-Interm on 0000 UTC 20 September. The red line shows the cruise track of the R/V Mirai in 2013. The white dot represents the FPO station. The study area in Figure 1a corresponds to the region indicated by the red square.

for Marine-Earth Science and Technology (JAMSTEC). During the surveys, we established an FPO station in the northern Chukchi Sea and remained there for about 2 weeks (10–26 September). At the FPO station, continuous surface meteorological observations, ocean microstructure measurements (2 times a day on 14–17 September and 3 times a day after that; some casts were canceled because of rough weather), and CTD/water sampling (every 6 h) were undertaken. CTD and expendable CTD (XCTD) surveys crossing the FPO station were also conducted once a day within a 16 km radius from the station (see the embedded map in Figure 1a). To understand flow fields around the FPO station, we launched two drifting buoys near the station on 17 September. The two buoys had drogues installed at 15 and 40 m, respectively, reflecting horizontal currents at the two depths. Detailed descriptions of data acquisition during the cruise are presented in the cruise report [*Nishino*, 2013], and the data will be released via the JAMSTEC Data Site for Research Cruises (http://www.godac.jamstec.go.jp/cruisedata/mirai/e/index.html). The following is an outline of how each observation was performed.

### 2.2. Surface Wind Observations

Surface meteorological parameters were observed throughout the cruise. We focused on wind speed and direction in this study (Figure 2a). These parameters were measured using an anemometer (KE-500, Koshin Denki, Japan) that was installed on the foremast of the ship at a height of 24 m above the sea surface. The data were averaged over 10 min periods.

### 2.3. Drifting Buoy

The drifting buoy (Zeni Lite Buoy Co., Ltd., Japan) consisted of a surface floating unit that included a GPS sensor and iridium communication system, and a holey-sock drogue installed at middepth, linked together with a fabric nylon rope. The rope length was determined so that it could capture the horizontal current at the chosen level. The GPS system sent hourly geographical information with almost 15 m

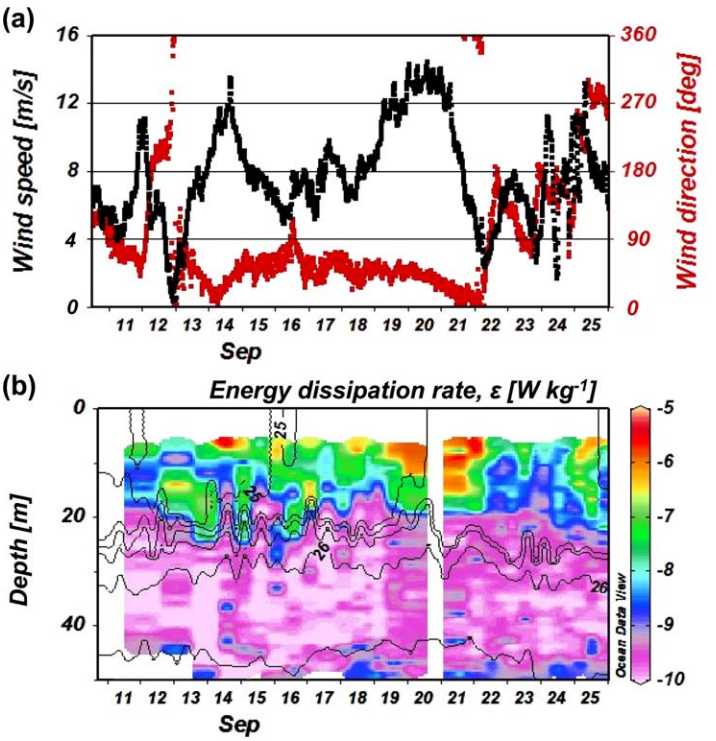


**Figure 2.** Time series of (a) wind speed (m $s^{-1}$; black) and direction rotating clockwise from the north (degrees; red), and (b) profiles of the kinetic energy dissipation rate, $\varepsilon$ (W $kg^{-1}$; color), at the FPO station. In Figure 2b, $\varepsilon$ is represented by a logarithmic scale, and the colored bar indicates the order of magnitude of $\varepsilon$. Contours of potential density are superimposed on the temporal evolution of $\varepsilon$. The potential density contours are from 24.75 to 26.25 with an interval of 0.25.

accuracy. The current measurement using the holey-sock drogue was considered accurate within 10% of the horizontal current magnitude [*Niiler et al.*, 1995; *Matsuno et al.*, 2006].

### 2.4. Ocean Microstructure Measurements

To measure ocean turbulent mixing and estimate the vertical fluxes of heat, salt, and nutrients, microscale (0.001–1 m) vertical shear data were collected using a Turbulent Ocean Microstructure Acquisition profiler (TurboMAP, JFE Advantech Co., Ltd., Japan), which was lowered from the surface to just above the bottom [*Wolk et al.*, 2002]. Within the top 7 m, the microscale data were not used in the analysis because they may have been affected by the initial adjustment to a free-falling state. The dissipation rate of turbulence kinetic energy, $\varepsilon$, was calculated from the small-scale current shear by integrating the energy spectrum in the wave number field. To estimate the vertical fluxes of heat, salt, and nutrients, the vertical eddy diffusivity, $K_\rho = \Gamma\varepsilon/N^2$, was calculated from $\varepsilon$ and the Brunt-Vaisälä frequency, $N$, where $\Gamma = 0.2$ is an efficiency factor. For the determination of $N$, temperature and salinity detected by TurboMAP-based CTD sensors were used after taking running-averages with a 5 m smoothing filter. The estimations of $\varepsilon$ and $K_\rho$ were described in detail by *Kawaguchi et al.* [2014].

### 2.5. CTD/Water Samplings

A CTD system (SBE9plus, Sea-Bird Electronics Inc., Bellevue, WA, USA) and a carousel water sampling system with 36 Niskin bottles (12 L) were used to make observations. Seawater samples were collected for measurements of salinity, dissolved oxygen, total alkalinity, nutrients (nitrate, nitrite, phosphate, silicate, and ammonia), total and size-fractionated chlorophyll *a*, primary productivity, and other chemical and biological parameters. The standard depths of collection were 5, 10, 20, 30, 40, 45, and 50 m at the FPO station (bottom depth = 56 m). At stations deeper than the FPO station, we also collected water samples from 75, 100, 125, 150, 175, 200, 225, 250, 300, 400, 500, 600, 800, 1000, 1500, 2000, and 2500 m, and a depth just above the seafloor. Surface water samples were also collected with a bucket.

Bottle salinity samples were analyzed following the Global Ocean Ship-based Hydrographic Investigations Program (GO-SHIP) Repeat Hydrography Manual using a Guildline AUTOSAL salinometer and International Association for the Physical Sciences of the Oceans standard seawater as a reference material [*Kawano*, 2010]. The precision of salinity measurements was 0.0068 for shallow-water samples ($\leq$200 m) and 0.0002 for deep water samples ($>$200 m).

Dissolved oxygen in the samples was measured by Winkler titration following the World Ocean Circulation Experiment Hydrographic Program operations and methods [*Dickson*, 1996]. The precision of dissolved oxygen measurements was 0.74 $\mu$mol $kg^{-1}$.

Total alkalinity in the samples was measured by a spectrophotometric system using the scheme reported by *Yao and Byrne* [1998]. The total alkalinity values were calibrated against a certified reference material provided by Dr. Dickson of the Scripps Institute of Oceanography. The precision of the total alkalinity was 0.8 $\mu$mol kg$^{-1}$.

Nutrient samples were analyzed according to the GO-SHIP Repeat Hydrography Manual [*Hydes et al*., 2010] using reference materials for nutrients in seawater [*Aoyama and Hydes*, 2010; *Sato et al*., 2010]. The precision, expressed as a coefficient of variation (CV), was 0.11% for nitrate, 0.19% for nitrite, 0.11% for phosphate, 0.16% for silicate, and 0.30% for ammonia.

Chlorophyll *a* in seawater samples was measured using a fluorometric nonacidification method [*Welschmeyer*, 1994] and a Turner Design fluorometer (10-AU-005). For size-fractionated chlorophyll *a* measurements, phytoplankton cells in the water samples were fractionated using three types of 47 mm diameter filters (pore sizes: 20, 10, and 2 $\mu$m) and a 25 mm diameter Whatman GF/F filter (pore size: $\sim$0.7 $\mu$m). Although the frequency of observations of total chlorophyll *a* at the FPO station was every 6 h (as for the other parameters described above), size-fractionated chlorophyll *a* was measured only once a day. The precision of chlorophyll *a* in terms of the CV was 7.4%.

The primary productivity of phytoplankton was determined using the stable $^{13}$C isotope method [*Hama et al*., 1983]. We sampled seawater from seven optical depths: at 100, 38, 14, 7, 4, 1, and 0.6% of the surface irradiance. The seawater samples were inoculated with a 200 $\mu M$ labeled carbon substrate (NaH$^{13}CO_3$) that represented $\sim$10% enrichment of the total inorganic carbon in the ambient water. The samples were placed in an incubator for 24 h. The temperature in the incubator was maintained with running water from the sea surface. After incubation, the water samples were filtered onto glass fiber filters (Whatman GF/F, 25 mm in diameter) that had been precombusted at 450°C for 4 h. The $^{13}$C measurements were performed onboard the ship using a stable-isotope analyzer (ANCA-SL, Europa Scientific Ltd.; now SerCon Ltd., Crewe, UK). The frequency of measurements was every other day. The precision of primary productivity in terms of the CV was 12%. Daily sea surface photosynthetically active radiation (PAR) was monitored with an LI-190SB air quantum sensor and recorded on an LI-1400 data logger (LI. COR Inc., Lincoln, NE, USA).

For water mass analyses, we used the fractions of sea-ice meltwater ($f_{SIM}$) and other freshwater ($f_{OF}$) calculated from the relationship between total alkalinity and salinity, based on the analysis reported by *Yamamoto-Kawai et al*. [2005]. They assumed that other freshwater included river runoff, precipitation, and freshwater carried by Pacific-origin water. The fraction of sea-ice meltwater, $f_{SIM}$, increases when seawater is influenced by sea-ice melt in summer and decreases when seawater is influenced by sea-ice formation in winter. A negative $f_{SIM}$ implies that sea-ice formation, which removes freshwater and ejects brine into seawater, is dominant over sea-ice melting.

### 2.6. XCTD

Probes of XCTD (Tsurumi-Seiki Co., Ltd., Japan) were launched from the stern of the ship into the sea to measure vertical profiles of temperature and salinity to a depth of 1000 m, or the sea bottom in cases where the bottom depth was less than 1000 m. The data were communicated back to a digital data converter and a computer onboard the ship by a fine wire, which is designed to break when the probe reaches its maximum depth. The precisions of the temperature and salinity measurements were 0.02°C and 0.04, respectively.

## 3. Results

### 3.1. Wind and Ocean Turbulent Mixing

The time series of wind speeds and directions during the FPO in the northern Chukchi Sea is shown in Figure 2a. There were three strong-wind events: the first lasted for a day around 14 September with northeasterly winds stronger than 10 m s$^{-1}$, the second occurred from 19–21 September with northeasterly winds stronger than 12 m s$^{-1}$, and the third was observed from 24–25 September with southeasterly to southwesterly winds stronger than 10 m s$^{-1}$. Sea level pressure (SLP) distribution on 20 September 2013, when the wind was strongest during the FPO period, is shown in Figure 1b.

The strong-wind events have enhanced turbulent mixing in the ocean. Figure 2b shows the time series of the vertical profile of the turbulent kinetic energy dissipation rate, $\varepsilon$. High $\varepsilon$ values, the order of which were

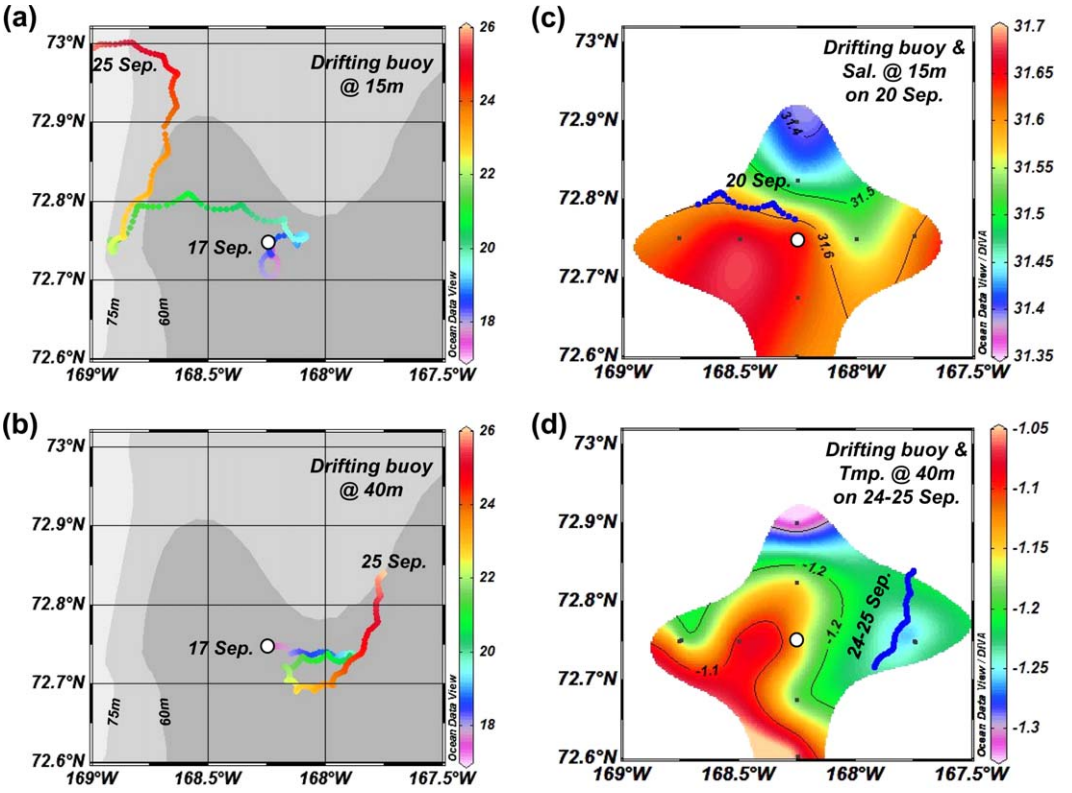


**Figure 3.** Drift tracks of the buoys with drogues set at (a) 15 m and (b) 40 m. Both the buoys were launched on 17 September near the FPO station (white dot). Color indicates the day of September. (c) Salinity distribution (color) at 15 m depth on 20 September and the track of the shallower-drogue buoy on that date (blue curve). Contours of salinity are 31.4, 31.5, and 31.6. (d) Temperature distribution (color) at 40 m depth on 24–25 September and the track of the deeper-drogue buoy on those dates (blue curve). Contours of temperature are −1.3, −1.2, and −1.1. In Figures 3c and 3d, the white dot represents the FPO station and the dots encompassing the FPO station are the CTD/XCTD stations shown in the embedded map in Figure 1a.

$10^{-7}-10^{-5}$ W kg$^{-1}$ and hereafter abbreviated as O ($10^{-7}-10^{-5}$) W kg$^{-1}$, at the surface (7–10 m) were observed during the periods corresponding to the strong-wind events. In particular, during the second event (19–21 September), when the highest wind speed during the FPO period occurred, the highest $\varepsilon$ values of O($10^{-6}-10^{-5}$) W kg$^{-1}$ were found down to a depth of 15 m. Furthermore, high $\varepsilon$ values of O ($10^{-7}-10^{-6}$) W kg$^{-1}$ were found during 12–16 September at depths near the pycnocline, which divided the water column into two layers. This magnified turbulent energy may have resulted from wind-induced internal waves that generated by semidiurnal inertial motion and propagated in a weakly stratified upper layer [*Kawaguchi et al*., 2015]. Below 20 m, although $\varepsilon$ decreased to O ($<10^{-10}$) W kg$^{-1}$ throughout the FPO period, values near the bottom often became relatively high with O ($10^{-9}-10^{-8}$) W kg$^{-1}$, suggesting the influence of vertical current shear near the seafloor.

### 3.2. Buoy Drifts

The motion of the drifting buoys seemed partly correlated with the wind speed and direction. We launched two buoys near the FPO station on 17 September, when the wind was weak. The buoy with a drogue at a depth of 15 m above the pycnocline was stagnant at the beginning (Figure 3a). After strong northeasterly winds on 19 September, the buoy started to move westward and attained its maximum speed (daily average: 0.18 m s$^{-1}$) on 20 September. Between 22 and 24 September, the buoy migrated rapidly to the northeast under southeasterly winds. The buoy then traveled toward the west along 73°N on 25 September, although the winds were southwesterly to westerly on this date.

Another buoy with a drogue at 40 m depth below the pycnocline moved even slower than the buoy with the drogue at 15 m depth (Figure 3b). The deeper-drogue buoy drifted eastward between 17 and 19 September. After 20 September, it moved westward in response to the northeasterly gale-force winds between 19 and 21 September, but slower than the shallower-drogue buoy. Between 22 and 23 September, when

the wind was weak, the buoy again drifted eastward, and subsequently traveled to the northeast under southeasterly to southwesterly strong winds on 24–25 September.

Vertical shear of horizontal velocities (namely, baroclinicity) between the upper and lower layers separated by the pycnocline might cause enhanced mixing around the pycnocline. The gradient Richardson number ($Ri = N_{pyc}^2/(\partial u/\partial z)^2$) became less than 1 due to the strong velocity shear at some point on 19–20 and 25 September during the strong-wind events, where $N_{pyc}$ ($\sim$0.015–0.025 $s^{-1}$) is the Brunt-Vaisälä frequency at the pycnocline and $\partial u/\partial z$ ($\sim$0.015–0.035 $s^{-1}$) is the velocity shear estimated from the motions of the above mentioned two buoys. However, the *Ri* was generally greater than 1, so that the density stratification around the pycnocline was strong enough to stabilize the entrainment due to the vertical current shear there [*Kawaguchi and Nishino*, 2014]. This is consistent with the result from the microstructure measurement, in which $\varepsilon$ was detected as generally small (i.e., $\varepsilon < O(10^{-9})$ W $kg^{-1}$) around the depth of the pycnocline (Figure 2b).

Note that for both buoys, a small-scale meandering motion was observed with an oscillation period of $\sim$12 h. This oscillation lasted throughout the FPO period and is attributed to inertial motions [*Kawaguchi et al*., 2015].

The motion of the drifting buoys illustrates the advection effect in the changes in the water characteristics at the FPO station. For example, although the motion of the shallower-drogue buoy indicated strong westward currents at 15 m on 20 September, a low salinity gradient in the zonal direction means that the currents were unable to contribute to change the water characteristics (Figure 3c). On the other hand, the rapid northeastward motion of the deeper-drogue buoy on 24–25 September, and a tongue-shaped structure of high temperature from the southwest, suggests a significant advection effect that was able to change the water characteristics at the FPO station (Figure 3d).

### 3.3. Hydrographic Profiles and Nutrients

As described in section 3.1, the water column at the FPO station was divided into two layers by the prominent pycnocline. The upper layer was characterized by warmer and fresher water than that of the lower layer (Figures 4a and 4b). Cooling of the upper layer occurred gradually during the FPO period, mainly due to atmospheric cooling, which is likely to be a typical seasonal change in Pacific-origin summer water [*Itoh et al*., 2013]. The temperature in the lower layer was almost constant and near freezing ($\sim -1.5$°C) except from 23–25 September, when warmer water ($\sim -1.0$°C) was present. The near-freezing water was identified as a remnant of Pacific-origin winter water that was formed by atmospheric cooling and brine rejection in previous winters [*Weingartner et al*., 2005]. Negative $f_{SIM}$ values in the lower layer are also evidence of brine rejection (Figure 4c).

Salinity in the upper layer was lowest on 11–14 September, during the FPO period. It increased significantly on 14 and 19 September and then remained almost constant. The lowest salinity in the upper layer on 11–14 September coincided with the highest $f_{SIM}$ value (Figure 4c). Therefore, the increase in salinity on 14 September would have been caused by a lateral discharge of sea-ice meltwater. On 19 September, the lateral advection effect would have been small because the shallower-drogue buoy was still stagnant at the onset of strong northeasterly winds (Figure 3a). The buoy then rapidly drifted westward on 20 September in response to the strong northeasterly winds. Nevertheless, the advection effect would have been small because the salinity distribution at 15 m depth showed a generally weak zonal salinity gradient (Figure 3c). Rather, lower salinity water just east of the FPO station would have been carried to the station by the westward currents. Regardless, the salinity at the FPO station increased in the upper layer. Therefore, the upward salt flux with enhanced vertical mixing because of the strong winds was the only source of increased salinity at the FPO station immediately after 19 September. The salinity in the lower layer was almost constant during the FPO period, except from 23–25 September when it decreased slightly.

On 23–25 September, warmer (and slightly fresher) water was present in the lower layer. At that time, the deeper-drogue buoy moved toward the northeast (Figure 3b), likely driven by the strong southeasterly to southwesterly winds. The northeastward currents carrying the buoy appeared to carry warm water from the southwest to the FPO station (Figure 3d). The intrusion of water with different characteristics at the FPO station was also evident in the $f_{OF}$ distribution; water with higher $f_{OF}$ values was present in the lower layer on 23–25 September (Figure 4d). In general, $f_{OF}$ values decrease with depth [*Yamamoto-Kawai et al*., 2005; *Nishino et al*., 2008], but here the maximum $f_{OF}$ value was at depths of 20–30 m.

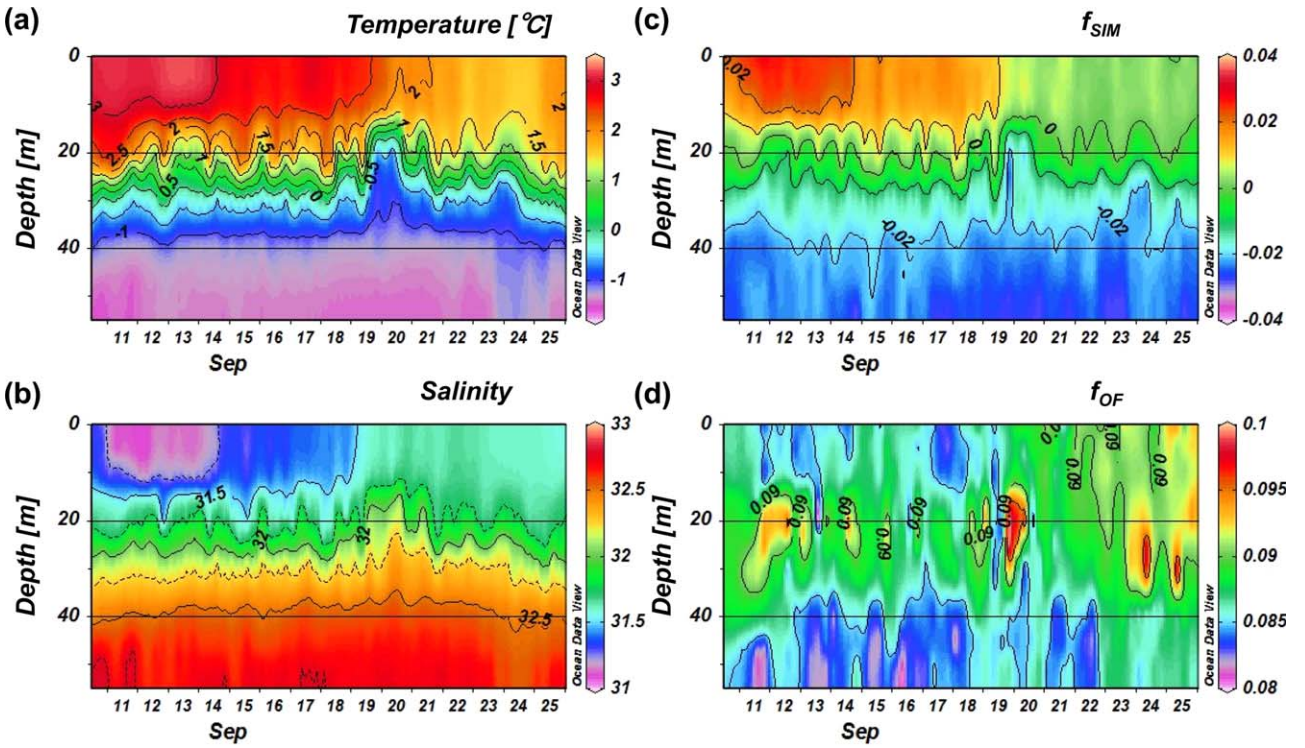


**Figure 4.** Time series of profiles of (a) temperature (°C), (b) salinity, (c) fraction of sea-ice meltwater, $f_{SIM}$, and (d) fraction of other freshwater, $f_{OF}$, at the FPO station. In Figure 4a, the contours of temperature are from −1 to 3, with an interval of 0.5. In Figure 4b, the contours of salinity are 31.25 (dashed), 31.5 (solid), 31.75 (dashed), 32 (solid), 32.25 (dashed), 32.5 (solid), and 32.75 (dashed). In Figure 4c, the contours of $f_{SIM}$ are from −0.02 to 0.02, with an interval of 0.01. In Figure 4d, contours of the $f_{OF}$ are from 0.085 to 0.095 with an interval of 0.005.

Total inorganic nitrogen (TIN = nitrate + nitrite + ammonia) and phosphate distributions (Figures 5a and 5b) indicate a two-layer structure throughout the FPO period, with lower concentrations in the upper layer and higher concentrations in the lower layer, separated by a nutricline that appeared at the level of the pycnocline. On 23–25 September, the TIN and phosphate concentrations in the lower layer decreased, suggesting intrusion of different water from the southwest, with low nutrient concentrations.

Silicate concentrations (Figure 5c) were also lower in the upper layer and higher in the lower layer, but they frequently showed a subsurface maximum at depths of 20–30 m, which corresponded in time with the $f_{OF}$ maximum at the same depth (Figure 4d). On 24 and 25 September, the subsurface silicate maximum deepened and merged with the high silicate concentrations of bottom water, but it was still possible to identify the subsurface silicate maximum with the $f_{OF}$ maximum. The subsurface silicate maximum is an unusual structure in the Chukchi Sea. In general, silicate concentrations increase with depth because the silicate is used to form diatom shells in the surface euphotic zone and is produced by dissolution of the shells deposited at the bottom of the Chukchi Sea.

To exaggerate the surface variation of nutrients, time series for TIN, phosphate, and silicate concentrations averaged over the surface to 10 m layer are shown in Figure 6. TIN was almost depleted throughout the FPO period ($<$0.15 $\mu$mol kg$^{-1}$). The temporal changes in phosphate concentrations indicated an increasing trend, with two peaks of maximum concentrations just after the first two strong-wind events: one was around 15 September and the other was during the period 20–22 September. The third strong-wind event on 24–25 September did not increase the phosphate concentrations. There are two possible reasons for the absence of a phosphate peak during the third event. First, the wind speed was lower in the third event than in the second event, and unlike the first and second events, the strong wind in the third event did not blow continuously. Second, the intrusion of lower nutrient water related to the strong currents (Figure 3a) might have reduced the phosphate concentrations. Similarly, two peaks of maximum concentrations were found in the time series of silicate just after the first two strong-wind events, and no peak was observed during the third strong-wind event. The higher silicate concentrations at the beginning of the FPO period may be

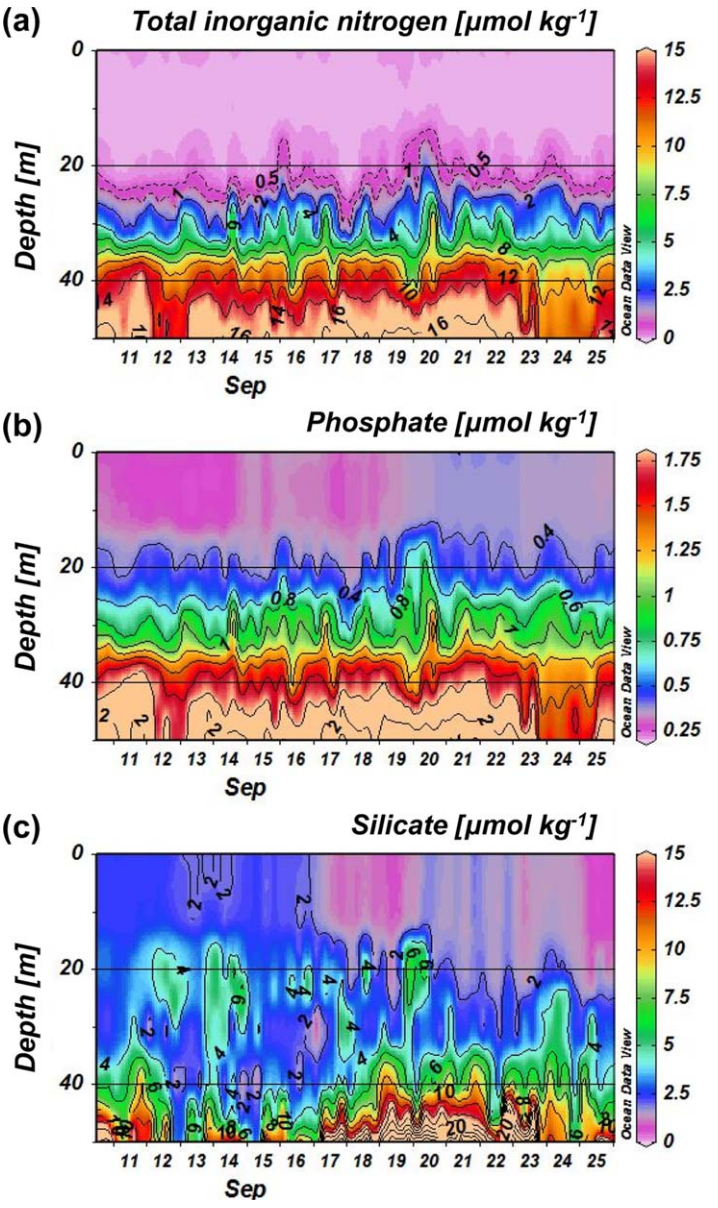


**Figure 5.** Time series of profiles of (a) total inorganic nitrogen ($\mu$mol kg$^{-1}$), (b) phosphate ($\mu$mol kg$^{-1}$), and (c) silicate ($\mu$mol kg$^{-1}$) at the FPO station. In Figure 5a, the contours of total inorganic nitrogen are 0.5 (dashed), 1 (dashed), and from 2 to 16 (solid), with an interval of 2. In Figure 5b, the contours of phosphate are from 0.4 to 2, with an interval of 0.2. In Figure 5c, the contours of silicate are from 2 to 24, with an interval of 2.

related to the influence of sea-ice meltwater that contained more silicate than other nutrients, such as the water observed under the sea ice in the Canada Basin [*Lee et al.*, 2010].

The nutrient peaks just after the first two strong-wind events were likely caused by increases in the upward nutrient fluxes due to enhanced turbulent mixing associated with the strong-wind events. We calculated the upward nutrient fluxes by multiplying the vertical gradients of nutrients obtained from the water samples by $K_\rho$ derived from the microstructure current shear (Figures 7a–7c). In the phosphate and silicate fluxes (Figures 7b and 7c), large values were observed at depths around 10 m just after and during the strong-wind events, especially the second event of 19–22 September. This suggests that the enhanced turbulent mixing caused by the strong-wind events increased the vertical fluxes of phosphate and silicate, resulting in peaks with high concentrations of phosphate and silicate (Figures 6b and 6c). The enhanced turbulent mixing due to strong winds could also increase the TIN flux at ~10 m (Figure 7a), but nitrogenous nutrients are a limiting factor for primary production in the Chukchi Sea [*Codispoti et al.*, 2005; *Tremblay and Gagnon*, 2009] and would be promptly exhausted by biological uptake. As a result, TIN continued to be depleted and did not have a peak with a high concentration even during the strong-wind event (Figure 6a). Note that high values of vertical nutrient fluxes were also found just above or in the pycnocline during the period 12–16 September, when internal waves caused significant disturbances through vertical propagation of kinetic energy [*Kawaguchi et al.*, 2015]. We also found high values of vertical nutrient fluxes near the bottom, where the turbulent mixing was relatively high (Figure 2b) and the nutrient concentrations increased significantly with depth (Figure 5).

### 3.4. Chlorophyll *a* and Primary Production

Time series of chlorophyll *a* concentrations in the water column at the FPO station and the ratio of large phytoplankton (>20 $\mu$m) chlorophyll *a* to the total chlorophyll *a* averaged over the surface to 10 m layer are shown in Figures 8a and 8b, respectively. Until 14 September, there was a subsurface chlorophyll *a* maximum

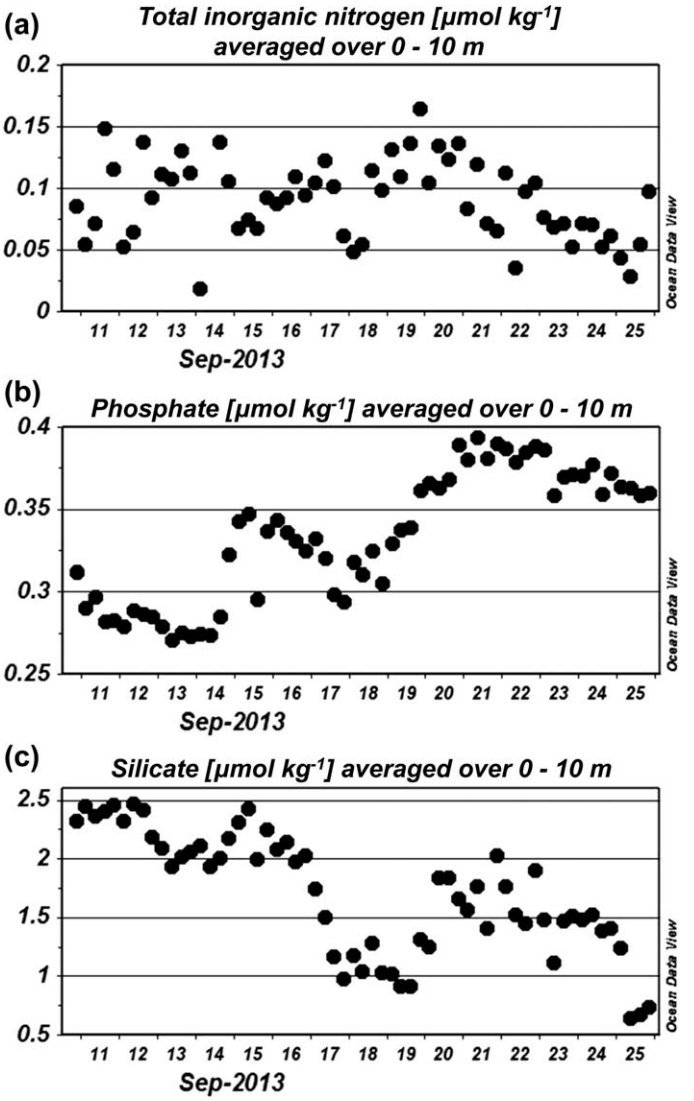


**Figure 6.** Time series of averaged concentrations over the surface 10 m for (a) total inorganic nitrogen ($\mu$mol kg$^{-1}$), (b) phosphate ($\mu$mol kg$^{-1}$), and (c) silicate ($\mu$mol kg$^{-1}$) at the FPO station.

at around 20 m, which is a typical structure of the chlorophyll *a* profile in postbloom conditions in the northern Chukchi Sea [*Hill and Cota*, 2005; *Ardyna et al.*, 2013]. At this time, the chlorophyll *a* concentration in the upper layer was the lowest during the whole FPO period ($\sim$0.3 $\mu$g L$^{-1}$). The lowest chlorophyll *a* level was likely related to the fresher water with a high $f_{SIM}$ that inhibited the upward nutrient fluxes from the pycnocline (nutricline). On 14 September, the surface chlorophyll *a* concentration increased, with a decrease in sea-ice meltwater and became almost homogeneous in the upper layer. On 16 and 17 September, the chlorophyll *a* concentration slightly increased at 20 m depth. This might be due partly to an increase in phytoplankton activity associated with the high nutrient fluxes caused by mixing via the internal waves around the pycnocline during the period 12–16 September (Figure 7). After 19 September, the chlorophyll *a* concentration in the upper layer significantly increased with time, through the strong-wind events accompanying the enhanced upward nutrient fluxes, and on 21 September it exceeded 0.8 $\mu$g L$^{-1}$, or 2.7 times higher than the initial concentration (0.3 $\mu$g L$^{-1}$).

In the lower layer, anomalously high chlorophyll *a* concentrations (>1 $\mu$g L$^{-1}$), which might be related to uplifted phytoplankton from the seafloor, were found at around 30 m, with semidiurnal oscillations on 18–19 and 23–25 September, suggesting lateral intrusions of high chlorophyll *a* water due to inertial motion of the water. Similar oscillations might also have occurred in the upper layer, but this was not clear because the water surrounding the FPO station would have had the same levels of chlorophyll *a* concentrations, which synchronously increased during the strong-wind events.

The fraction of large phytoplankton chlorophyll *a* also increased with the increase in the surface chlorophyll *a* concentration (Figure 8b), reflecting the fact that the upward nutrient fluxes enhanced by the strong winds contributed to improved nutrient conditions in the upper layer. According to the microscopic observations, the increased amounts of large phytoplankton in the later FPO period were mainly due to *Proboscia eumorpha*, which is a chain-forming diatom with an elongated cylindrical frustule.

Time series of primary productivity and of total daily PAR at the sea surface during the FPO period are shown in Figures 9a and 9b, respectively. In general, primary productivity decreased with depth and the integrated productivity over the water column (56 m) was lowest (84 mg C m$^{-2}$ d$^{-1}$) on 14 September and highest (166 mg C m$^{-2}$ d$^{-1}$) on 22 September. Until 14 September, the primary productivity in the water

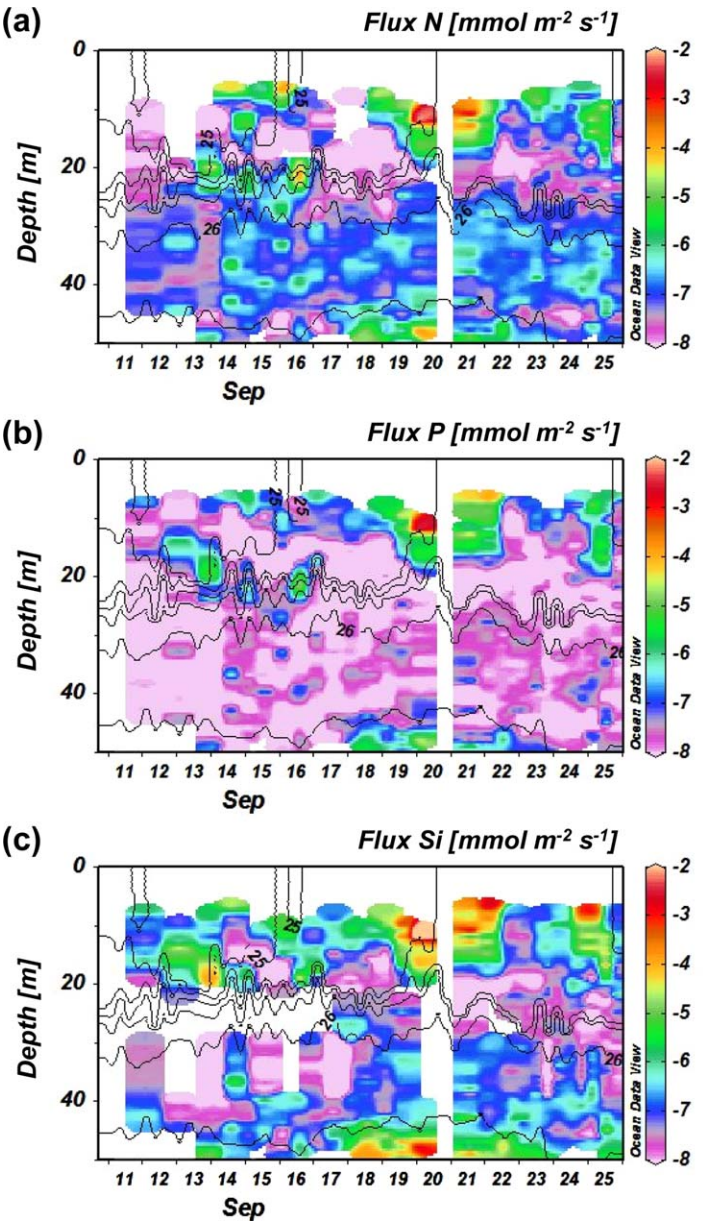


**Figure 7.** Time series of profiles of upward fluxes for (a) total inorganic nitrogen (mmol $m^{-2}$ $s^{-1}$), (b) phosphate (mmol $m^{-2}$ $s^{-1}$), and (c) silicate (mmol $m^{-2}$ $s^{-1}$) at the FPO station. In each figure, the upward flux is represented by a logarithmic scale, and the colored bar indicates the order of magnitude of the upward flux. Contours of potential density are superimposed on the temporal evolution of the upward flux. The potential density contours are from 24.75 to 26.25, with an interval of 0.25.

column decreased with time (Figure 9a) and the total daily PAR at the sea surface displayed a decreasing trend over this period (Figure 9b). At this time, TIN was depleted (Figure 5a) and the upward flux of TIN was low (Figure 7a). Therefore, TIN available for primary production would have been regenerated in the upper layer. TIN regeneration was consistent with the predominance of small phytoplankton at this time (Figure 8b). After 14 September, the primary productivity in the water column increased with time, reaching a maximum on 22 September (Figure 9a), despite the PAR being lower than at the beginning of the FPO period (Figure 9b). The increase in productivity was likely a biological response to the enhanced upward fluxes of nutrients due to the strong winds. This effect doubled the primary productivity (84 mg C $m^{-2}$ $d^{-1}$ on 14 September to 166 mg C $m^{-2}$ $d^{-1}$ on 22 September). By compiling chlorophyll *a* data in the Arctic Ocean and then applying an empirical model, *Ardyna et al*. [2013] found fall blooms that were assumed to have resulted from storms, surface cooling, and sea-ice formation. Based on satellite data, *Ardyna et al*. [2014] also suggested more frequent fall blooms throughout the Arctic Ocean due to recent sea-ice loss. The observations reported here reveal that increases in chlorophyll *a* and primary productivity would have been associated with the fall bloom, with evidence of small-scale mixing due to strong winds.

## 4. Discussion

### 4.1. Mixing Process and Its Impact on Biological Activity

At the beginning of the FPO period (until 14 September), water with a high $f_{SIM}$ occupied the upper layer, producing a weak stratification above the pycnocline (Figures 4b and 4c). Due to this weak stratification, the energy of the internal wave packet was able to propagate in the upper layer, forcing internal mixing above the pycnocline [*Kawaguchi et al*., 2015]. The significant turbulent mixing resulted in an increase in nutrient fluxes around the pycnocline during the period 12–16 September (Figure 7). Such large nutrient fluxes were 1 order of

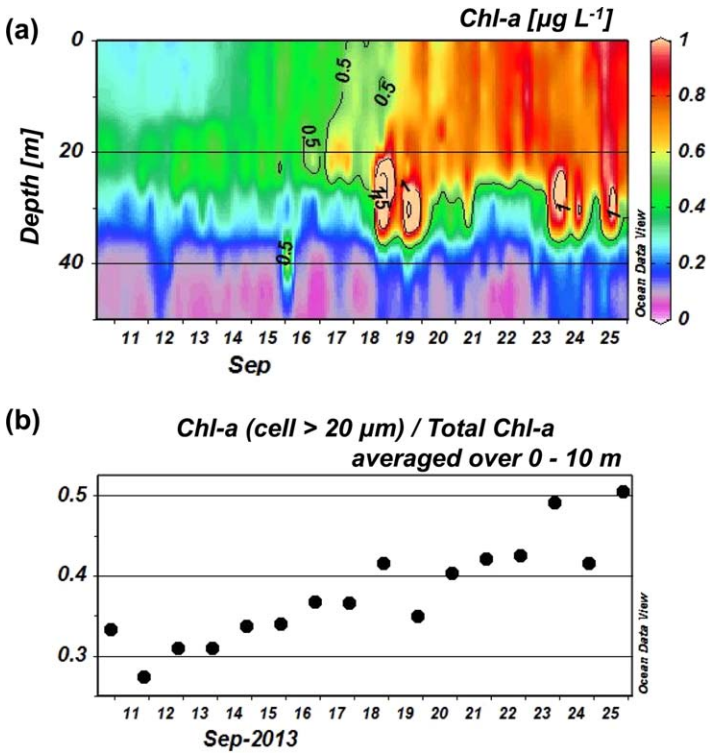


**Figure 8.** Time series of (a) profiles of chlorophyll *a* ($\mu$g L$^{-1}$) and (b) the ratio of large phytoplankton (>20 $\mu$m) chlorophyll *a* to the total chlorophyll *a* averaged in the surface (10 m) layer at the FPO station. In Figure 8a, the contours of chlorophyll *a* are from 0.5 to 1.5, with an interval of 0.5.

magnitude smaller than the fluxes associated with direct ocean mixing by strong winds. This is likely because the occurrence of internal waves was only episodic and intermittent. However, the internal wave might have been a contributing factor to the increase in chlorophyll *a* around the pycnocline at ~20 m depth on 16–17 September (Figure 8a). *Rainville et al.* [2011] suggested an increase in internal wave influence with recent sea-ice loss and, consequently, its possible impact on phytoplankton growth. Our results also indicate that the internal wave mixing could increase the upward nutrient fluxes and have a potential to influence the phytoplankton growth in a weakly stratified layer above the pycnocline that was covered by low-salinity water such as sea-ice meltwater.

During the FPO period, there were several strong-wind events (Figure 2a) that enhanced the turbulent mixing (Figure 2b) and increased the upward fluxes of nutrients (Figure 7), resulting in increased nutrient concentrations in the surface layer (0–10 m; Figure 6). Here we estimate the nutrient supply to the surface layer from these upward nutrient fluxes, and compare it to the nutrient consumption during phytoplankton growth. We obtained the largest nutrient fluxes at the base of the surface layer (10–13 m) between 19 and 20 September, and the average upward fluxes of TIN, phosphate, and silicate at this location were $4.0 \times 10^{-5}$, $4.0 \times 10^{-5}$, and $7.9 \times 10^{-4}$ mmol m$^{-2}$ s$^{-1}$, respectively (Figure 7). These nutrient fluxes were observed during an uplifted pycnocline (see contours in Figure 7). The pycnocline surface was oscillating vertically at a period ~12 h, which was close to the local inertial period (12.53 h at 72.75°N). Therefore, the TIN, phosphate, and silicate supplied to the surface layer by the combination of strong turbulent mixing and the uplifted pycnocline during 12 h between 19 and 20 September were 1.7, 1.7, and 34 mmol m$^{-2}$, respectively. These nutrient supplies resulted in the most prominent increases in phosphate and silicate concentrations, which occurred on 19–20 September and maintained high concentrations until 22 September (Figures 6b and 6c), under the strongest wind event during the FPO period (Figure 2a).

Nutrient consumption during phytoplankton growth was estimated from the primary productivity. The integrated productivity over the surface-to-10 m layer averaged between 20 and 22 September was 70 mg C m$^{-2}$ d$^{-1}$. This was when the highest productivity was observed during the FPO period due to the influence of the strongest wind event and nutrient supply, as described above. The assimilation rates of nutrients estimated using the Redfield-Brzezinski nutrient ratio (C:N:P:Si = 106:16:1:15) [*Brzezinski*, 1985] were 0.88, 0.055, and 0.83 mmol m$^{-2}$ d$^{-1}$ for TIN, phosphate, and silicate, respectively. The ratio of the carbon to nitrogen uptake rate observed in the Chukchi Sea was 4.6–5.0 [*Lee et al.*, 2007], slightly lower than the Redfield-Brzezinski nutrient ratio (C/N = 6.6). The total nutrient consumption during phytoplankton growth in the period 19–22 September (4 days), when the most prominent increases in phosphate and silicate concentrations occurred under the strongest wind event, were 3.5, 0.22, and 3.3 mmol m$^{-2}$ for TIN, phosphate, and silicate, respectively. By comparing these values for biological nutrient consumption with the nutrient levels

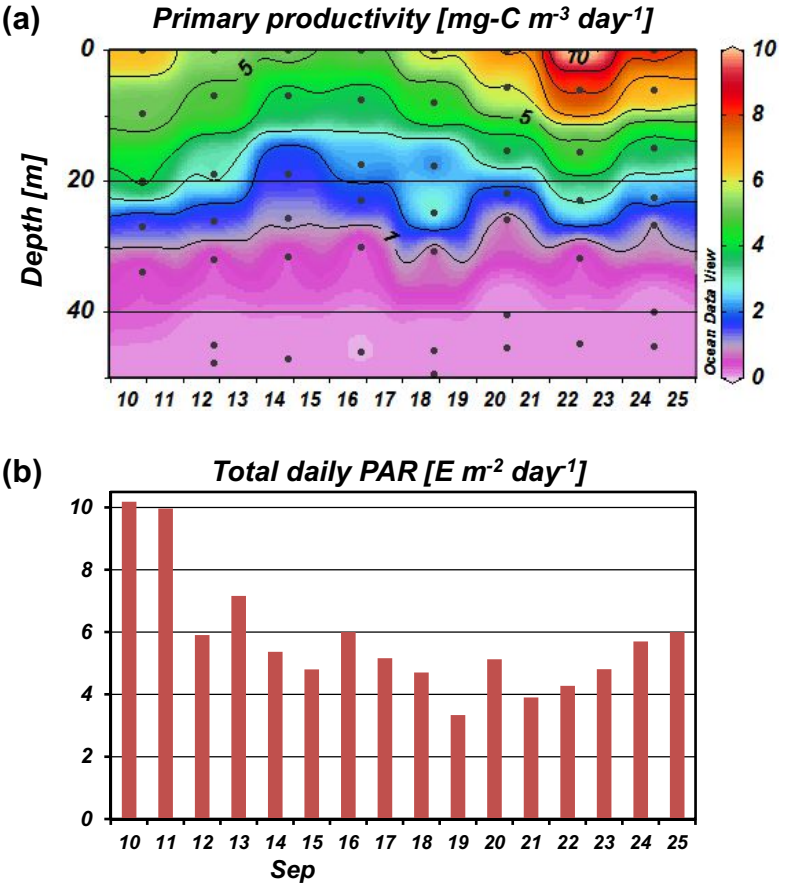


**Figure 9.** Time series of (a) profiles of primary productivity (mg C $m^{-3}$ $d^{-1}$) and (b) total daily photosynthetically active radiation (PAR) (E $m^{-2}$ $d^{-1}$) on the deck of the ship at the FPO station. In Figure 9a, the data sampling levels are indicated by black dots, and the sampling was conducted every other day. The contours of primary productivity are from 1 to 10, with an interval of 1.

supplied by the strong-wind-induced turbulent mixing, it was observed that the TIN supply (1.7 mmol $m^{-2}$) and consumption (3.5 mmol $m^{-2}$) were roughly comparable. However, the phosphate and silicate supplies (1.7 and 34 mmol $m^{-2}$, respectively) were an order of magnitude larger than the biological consumption (0.22 and 3.3 mmol $m^{-2}$, respectively). Some of the nutrients assimilated by phytoplankton were regenerated in the surface layer, and therefore the estimated biological consumption was considered the maximum case. As a result, the TIN supplied by the strong-wind-induced turbulent mixing was considered to be promptly consumed during phytoplankton growth in the surface layer, but the phosphate and silicate supplies were much larger than the biological consumption, resulting in the increase in phosphate and silicate in the surface layer under the strongest wind event. After biological consumption was subtracted, the increases in phosphate and silicate in the surface layer (10 m) due to supplied nutrient were calculated to be 0.15 and 3.1 $\mu$mol $kg^{-1}$, respectively, which explained the observed increase in phosphate ($\sim$0.1 $\mu$mol $kg^{-1}$) and silicate ($\sim$0.9 $\mu$mol $kg^{-1}$) during the period 19–22 September, under the strongest wind event. Similarly, the estimated increase in salinity ($\sim$0.4) in the surface layer caused by upward salt flux due to mechanical mixing associated with the strongest wind event accounted for the observed increase in salinity ($\sim$0.2) during the event.

Upward nutrient fluxes near the bottom were relatively high, with maximum values occurring on 20 September (Figure 7), when northeasterly wind speeds were above 12 m $s^{-1}$ (Figure 2a) and the deeper-drogue buoy moved rapidly westward (Figure 3b). The rapid buoy motion suggests a strong vertical velocity shear at the bottom, producing a high level of turbulent mixing there (Figure 2b) and resulting in large nutrient fluxes from the bottom (Figure 7). The present study, however, did not detect increases in primary productivity and phytoplankton biomass associated with enhanced bottom nutrient fluxes. However, if the wind had been even stronger, the bottom nutrient fluxes combined with the deep mixing by the wind

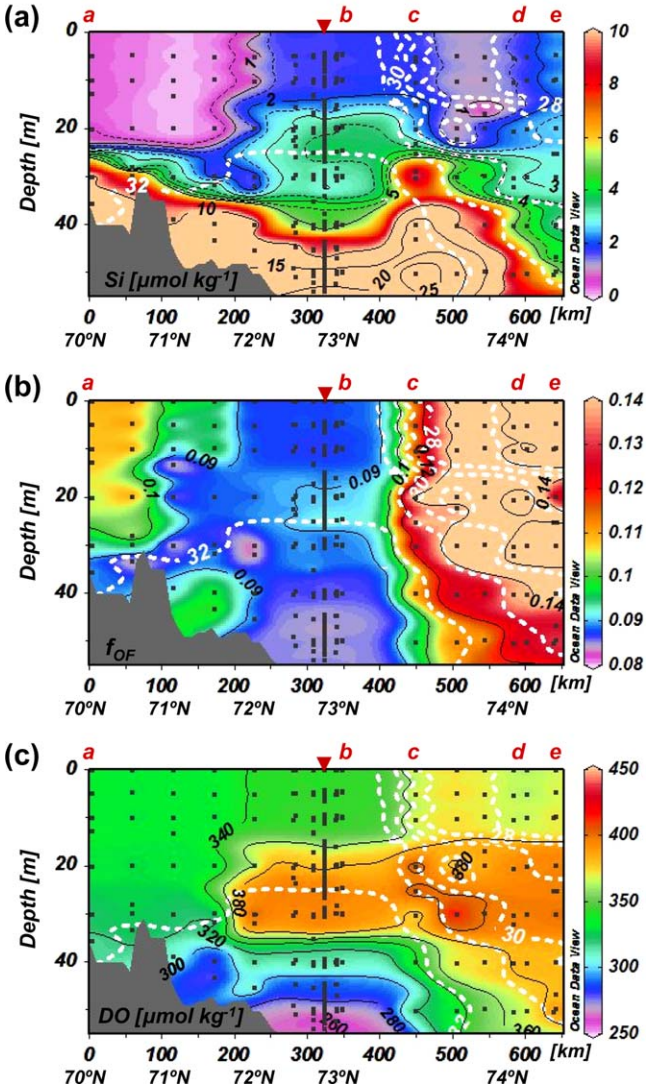


**Figure 10.** Vertical sections of (a) silicate ($\mu$mol kg$^{-1}$), (b) fraction of other freshwater than sea-ice meltwater, $f_{OF}$, and (c) dissolved oxygen ($\mu$mol kg$^{-1}$) from the Chukchi shelf to the Canada Basin via the positions of a, b, c, d, and e on the map in Figure 1a. The positions are displayed at the top of each figure and the location of the FPO station is marked by an inverted triangle at the top of each figure. The numbers at the bottom of each figure are the distance (km) from position a. Latitudes of the horizontal axis are also displayed at the bottom of each figure. The data used for the illustration of the vertical sections were obtained from the stations on the map in Figure 1a, and the data around the FPO stations were zonally and temporally averaged, excluding the data from 21–25 September when the subsurface silicate maximum at 20–30 m was not significant (see Figure 5c). At each station, the data sampling levels are indicated by black dots. In Figure 10a, the contours of silicate are from 0.5 to 5, with an interval of 0.5, and from 5 to 20, with an interval of 5. In Figure 10b, the contours of the $f_{OF}$ are from 0.09 to 0.10, with an interval of 0.01, and from 0.10 to 0.16, with an interval of 0.02. In Figure 10c, the contours of dissolved oxygen are from 260 to 400, with an interval of 20. In each figure, the white dotted lines indicate salinity contours from 27 to 32, with an interval of 1.

might have increased the primary productivity and phytoplankton biomass, resulting in a decrease in nutrients in the whole water column. This event might contribute to increasing the net community production (NCP) estimated from the changes in nutrient inventories in the whole water column, but the NCP estimation over the full water column is compromised by bottom processes such as remineralization, denitrification, and anammox [*Mordy et al*., 2012].

### 4.2. Source of a Subsurface Silicate Maximum

Although primary productivity is limited by TIN in the Chukchi Sea [*Codispoti et al*., 2005; *Tremblay and Gagnon*, 2009] and at the FPO station, the silicate supply is important for the growth of diatoms, which were identified by microscope observations at the FPO station. The silicate concentrations in the upper layer at the FPO station were less than 2 $\mu$mol kg$^{-1}$ after 17 September, and ~2 $\mu$mol kg$^{-1}$ before that date, when an influence of sea-ice meltwater that might have had a relatively high silicate level was found (Figure 5c). For the growth of diatoms, the silicate concentration should be more than the 2 $\mu$mol kg$^{-1}$ observed in mesocosm experiments [*Egge and Aksnes*, 1992], which were consistent with field studies in polar seas [e.g., *Poulsen and Reuss*, 2002; *Debes et al*., 2008]. Therefore, diatom growth that would have increased after the strong-wind events on 14 and 19–21 September at the FPO station (Figure 8b) is likely to have been sustained by silicate supplied from the subsurface silicate maximum at depths of 20–30 m. The vertical double silicate maximum, which was found at the subsurface (20–30 m) and at the bottom (~60 m) of the northern Chukchi Sea, is first reported here in the present study. *Nishino et al*. [2009] also reported a vertical double silicate maximum on the Siberian side of the Chukchi shelf slope. In their study, one silicate maximum corresponded to the shelf bottom water (salinity ($S$) = 32–32.5) and the other was formed by diatom shell dissolution on the shelf slope at the level of lower halocline water ($S$ = 34–34.5) [*Jones and Anderson*, 1986]. In our study, the bottom silicate maximum was formed by the dissolution of diatom shells that

had accumulated at the bottom of the Chukchi Sea [*Walsh et al.*, 1989]. However, the formation mechanism of the subsurface silicate maximum is unknown.

To elucidate the formation mechanism of the subsurface silicate maximum, we compared the distributions of silicate with other parameters. Figure 10 shows the vertical sections of silicate, $f_{OF}$, and dissolved oxygen from the Chukchi Sea to the Canada Basin via the FPO station. Over the central Chukchi Sea (70°N–72°N), the silicate concentration in the upper layer (0–20 m) was extremely low ($<1$ $\mu$mol kg$^{-1}$; Figure 10a), because the location is distant from a plume of high nutrient concentrations via the Bering Strait [*Springer and McRoy*, 1993]. The surface silicate concentration over the northern Chukchi Sea including the FPO station (72°N to position c in Figure 10a) was higher than in the central Chukchi Sea and this might result in higher primary productivity in this region than in the central Chukchi Sea [*Hill and Cota*, 2005]. The higher silicate concentrations in this region are likely related to the upwelling of nutrient-rich water. In the region from the Chukchi shelf slope to the Canada Basin (north of position c), the surface silicate concentration was low, but it increased toward the north, probably because silicate was supplied with sea-ice meltwater [*Lee et al.*, 2010]. Extremely high silicate concentrations ($>15$ $\mu$mol kg$^{-1}$) were found at the bottom of the northern Chukchi Sea. The water there was near freezing and had negative values of $f_{SIM}$ (not shown) and was previously identified as Pacific-origin winter water that remained on the shelf in late summer/fall, resulting in an increase in nutrients due to the remineralization of organic matter deposited at the bottom [*Codispoti et al.*, 2005; *Nishino et al.*, 2005]. Around the FPO station (72.75°N), a subsurface silicate maximum occurred at depths of 20–30 m and seemed to spread from a halocline ($S \sim 30$–$32$) below the surface water with extremely low salinity ($S < 30$) in the Canada Basin.

As described in section 3.3, the subsurface silicate maximum at the FPO station corresponded to the subsurface maximum of the $f_{OF}$ that also seems to have spread from the Canada Basin, where $f_{OF}$ values were extremely high (Figure 10b). The high $f_{OF}$ values in the Canada Basin water resulted from the convergence of surface freshwater within the Beaufort Gyre [e.g., *Proshutinsky et al.*, 2009]. Water with high $f_{OF}$ values was also found in the upper layer of the Chukchi Sea south of 72°N, but the silicate concentration there was extremely low and was different from the subsurface silicate maximum water. Water with high $f_{OF}$ values was also unaccountably found at the bottom of the Chukchi Sea, around 71.5°N. However, the subsurface silicate maximum water with high $f_{OF}$ values differed from the shelf bottom water, as described below.

Dissolved oxygen can be used to characterize the shelf bottom water, because oxygen is used in the decomposition of organic matter deposited on the bottom of the shelf. The water with high $f_{OF}$ values at the bottom of the Chukchi Sea, around 71.5°N, had a low oxygen content ($<300$ $\mu$mol kg$^{-1}$; Figure 10c). However, the subsurface silicate maximum water at the FPO station was characterized by a high oxygen content ($>380$ $\mu$mol kg$^{-1}$), and therefore it did not originate from the bottom water. Water with high oxygen concentrations corresponding to the subsurface silicate maximum likely originated in the Canada Basin, where oxygen concentrations were high even at deep levels. The deep penetration of oxygen-rich water in the Canada Basin is consistent with ventilation caused by surface water convergence and the Ekman pumping that drives the Beaufort Gyre. As a result, the subsurface silicate maximum water with high oxygen concentrations observed at the FPO station would have been derived from the ventilated halocline of $S \sim 30$–$32$ in the Canada Basin. The subsurface oxygen maximum ($>380$ $\mu$mol kg$^{-1}$) found around the FPO station and in the Canada Basin would be partly associated with subsurface phytoplankton growth [*Codispoti et al.*, 2005]. However, in the upper layer at the FPO station, the increase in phytoplankton biomass that accompanied strong-wind events caused little increase in oxygen concentrations. Therefore, the subsurface oxygen maximum at the FPO station was not produced by local phytoplankton growth during the FPO period. The oxygen maximum might be a remnant of a previous phytoplankton bloom and/or resulted from the spread of oxygen-rich water from the Canada Basin. Because the subsurface silicate, $f_{OF}$, and oxygen maxima were observed throughout the FPO period, the halocline water in the Canada Basin with high silicate and oxygen concentrations and high $f_{OF}$ values was assumed to have upwelled into the FPO station before the onset of the FPO program.

In addition to the strong-wind events, an upwelling event, which was not observed during the FPO period but occurred before the onset of the FPO program, would also play an important role in primary productivity and in determining the species of phytoplankton present. Upwelling is likely to be promoted in summer when the ice edge retreats beyond the shelf break [*Carmack and Chapman*, 2003] and the Beaufort Gyre circulation is enhanced [*Yang*, 2009]; therefore, it would be strongly affected by global warming and associated climate change. Upwelling events probably determine background stratification and nutrient distributions, and strong-wind events could control instantaneous vertical nutrient fluxes and biological

responses. Further studies are required to investigate the background stratification and nutrient distributions that must be associated with shelf-basin water exchanges and may impact biological activity in the northern Chukchi Sea. Moreover, there is a need to extend the current study to basin areas, where surface stratification is stronger and the nutricline is deepening [*McLaughlin and Carmack*, 2010] or shoaling [*Nishino et al*., 2013] with the recent sea-ice loss, to elucidate ocean and biological responses to atmospheric events throughout the Arctic Ocean.

## 5. Summary

We examined ocean and biological responses to atmospheric events, such as strong winds during autumn 2013, at an FPO station in the northern Chukchi Sea, where the water column consisted of a warmer/fresher/nutrient-poor upper layer and a colder/salter/nutrient-rich lower layer separated by a pycnocline. The 2 week observation period included three strong-wind events that enhanced vertical mixing. High-temporal-resolution hydrographic surveys and microstructure measurements enabled us to estimate vertical nutrient fluxes and the impact on biological activity of different types of turbulent mixing, such as that related to internal waves and direct ocean mixing near the surface by strong winds.

The largest nutrient fluxes during the FPO period were caused by a combination of enhanced turbulent mixing by strong winds and an uplifted pycnocline. The oscillation of pycnocline surfaces likely resulted from inertial motion of the water. Our temporally high-resolution surveys successfully captured the effect of this combination of factors on the increase in surface nutrients and concurrent increases in primary productivity and phytoplankton biomass, in particular large phytoplankton such as diatoms. This is the first observational evidence that wind-driven ocean mixing can impact biological activity in the Pacific Arctic, where low-salinity water from the Pacific Ocean, river water, and sea-ice meltwater produce a strong pycnocline that stabilizes the water column. Our observations also suggest that convective mixing associated with internal waves in the weakly stratified layer above the pycnocline can increase the upward nutrient fluxes from the pycnocline and may have an impact on biological activity there.

Our study sheds further light on the maintenance of biological activity in a nutrient-depleted region of the Arctic Ocean, the northern Chukchi Sea. Nitrogenous nutrients are a limiting factor for primary production in that region, but silicate supplied from the subsurface silicate maximum may play an important role in diatom production. The distributions of chemical tracers from the Chukchi Sea to the Canada Basin suggest that the subsurface silicate maximum water in the northern Chukchi Sea might be derived from the ventilated halocline in the Canada Basin, which is characterized by high concentrations of silicate and dissolved oxygen, and high $f_{OF}$ values.

**Acknowledgments**

We thank the captain, officers, and crew of the R/V Mirai, which was operated by Global Ocean Development, Inc. We also thank the staff of Marine Works Japan, Ltd. for their skillful work aboard the ship and for data processing. This study was partly supported by the Green Network of Excellence Program (GRENE Program), which is funded by the Arctic Climate Change Research Project of the Ministry of Education, Culture, Sports, Science, and Technology of Japan (MEXT). Maps and figures were drawn using Ocean Data View software [*Schlitzer*, 2015]. We thank the editor and two anonymous reviewers for their constructive comments, which helped us improve the manuscript. The data used to prepare this paper will be released via the JAMSTEC Data Site for Research Cruises (http://www.godac.jamstec.go.jp/cruisedata/mirai/e/index.html).

## References

Aagaard, K., and E. C. Carmack (1989), The role of sea ice and other fresh water in the Arctic circulation, *J. Geophys. Res.*, *94*, 14,485–14,498.

Aoyama, M., and D. J. Hydes (2010), How do we improve the comparability of nutrient measurements?, in *Comparability of Nutrients in the World's Ocean*, edited by M. Aoyama et al., pp. 1–10, Mother Tank, Tsukuba, Japan.

Ardyna, M., M. Babin, M. Gosselin, E. Devred, S. Bélanger, A. Matsuoka, and J.-É. Tremblay (2013), Parameterization of vertical chlorophyll *a* in the Arctic Ocean: Impact of the subsurface chlorophyll maximum on regional, seasonal, and annual primary production estimates, *Biogeosciences*, *10*, 4383–4404, doi:10.5194/bg-10-4383-2013.

Ardyna, M., M. Babin, M. Gosselin, E. Devred, L. Rainville, and J.-É. Tremblay (2014), Recent Arctic Ocean sea ice loss triggers novel fall phytoplankton blooms, *Geophys. Res. Lett.*, *41*, 6207–6212, doi:10.1002/2014GL061047.

Brzezinski, M. A. (1985), The Si:C:N ratio of marine diatoms: Interspecific variability and the effect of some environmental variables, *J. Phycol.*, *21*, 347–357.

Carmack, E., and D. C. Chapman (2003), Wind-driven shelf/basin exchange on an Arctic shelf: The joint roles of ice cover extent and shelf-break bathymetry, *Geophys. Res. Lett.*, *30*(14), 1778, doi:10.1029/2003GL017526.

Carmack, E., and P. Wassmann (2006), Food webs and physical-biological coupling on pan-Arctic shelves: Unifying concepts and comprehensive perspectives, *Prog. Oceanogr.*, *71*, 446–477, doi:10.1016/j.pocean.2006.10.004.

Chang, J., C. Chung, and G. Gong (1996), Influences of cyclones on chlorophyll *a* concentration and Synechococcus abundance in a subtropical western Pacific coastal ecosystem, *Mar. Ecol. Prog. Ser.*, *140*, 199–205.

Chung, C. C., G. C. Gong, and C. C. Hung (2012), Effect of Typhoon Morakot on microphytoplankton population dynamics in the subtropical Northwest Pacific, *Mar. Ecol. Prog. Ser.*, *448*, 39–49, doi:10.3354/meps09490.

Coachman, L. K., K. Aagaard, and R. B. Tripp (1975), *Bering Strait: The Regional Physical Oceanography*, 172 p., Univ. of Wash. Press, Seattle.

Codispoti, L. A., C. Flagg, V. Kelly, and J. H. Swift (2005), Hydrographic conditions during the 2002 SBI process experiments, *Deep Sea Res., Part II*, *52*, 3199–3226, doi:10.1016/j.dsr2.2005.10.007.

Comiso, J. C., C. L. Parkinson, R. Gersten, and L. Stock (2008), Accelerated decline in the Arctic sea ice cover, *Geophys. Res. Lett.*, *35*, L01703, doi:10.1029/2007GL031972.

Debes, H., E. Gaard, and B. Hansen (2008), Primary production on the Faroe shelf: Temporal variability and environmental influences, *J. Mar. Syst.*, *74*, 686–697, doi:10.1016/j.jmarsys.2008.07.004.

Dickson, A. G. (1996), Determination of dissolved oxygen in sea water by Winkler titration, in *WOCE Operations Manual, vol. 3, Sec. 3.1, Part 3.1.3 WHP Operations and Methods, WHP Off. Rep. WHPO 91-1, WOCE Rep. 68/91, Nov. 1994, Revision 1*, 13 pp., Woods Hole, Mass.

Egge, J. K., and D. L. Aksnes (1992), Silicate as regulating nutrient in phytoplankton competition, *Mar. Ecol. Prog. Ser.*, *83*, 281–289.

Hama, T., T. Miyazaki, Y. Ogawa, T. Iwakuma, M. Takahashi, A. Otsuki, and S. Ichimura (1983), Measurement of photosynthetic production of a marine phytoplankton population using a stable $^{13}C$ isotope, *Mar. Biol.*, *73*, 31–36.

Hill, V., and G. Cota (2005), Spatial patterns of primary production on the shelf, slope and basin of the Western Arctic in 2002, *Deep Sea Res., Part II*, *52*, 3344–3354, doi:10.1016/j.dsr2.2005.10.001.

Hung, C. C., and G. C. Gong (2011), Biogeochemical responses in the southern East China Sea after typhoons, *Oceanography*, *24*, 42–51, doi:10.5670/oceanog.2011.93.

Hydes, D. J., et al. (2010), Determination of dissolved nutrients (N, P, Si) in seawater with high precision and inter-comparability using gas-segmented continuous flow analysers, in *The GO-SHIP Repeat Hydrography Manual: A Collection of Expert Reports and Guidelines, IOCCP Rep. 14, ICPO Publ. Ser. 134*, edited by E. M. Hood, C. L. Sabine, and B. M. Sloyan, UNESCO-IOC, Paris, France. [Available at www.go-ship.org/HydroMan.html.]

Itoh, M., S. Nishino, Y. Kawaguchi, and T. Kikuchi (2013), Barrow Canyon volume, heat, and freshwater fluxes revealed by long-term mooring observations between 2000 and 2008, *J. Geophys. Res. Oceans*, *118*, 4363–4379, doi:10.1002/jgrc.20290.

Jones, E. P., and L. G. Anderson (1986), On the origin of the chemical properties of the Arctic Ocean halocline, *J. Geophys. Res.*, *91*, 10,759–10,767.

Kawaguchi, Y., and S. Nishino (2014), An observational study of ocean currents and an eddy in the Arctic Ocean using drifting buoys with drogues at selected depths: Trial experiments during R/V Mirai Arctic cruise in 2013 [in Japanese with English abstract], *JAMSTEC Rep. Res. Dev.*, *18*, 29–39.

Kawaguchi, Y., T. Kikuchi, and R. Inoue (2014), Vertical heat transfer based on direct microstructure measurements in the ice-free Pacific-side Arctic Ocean: The role and impact of the Pacific water intrusion, *J. Oceanogr.*, *70*, 343–353, doi:10.1007/s10872-014-0234-8.

Kawaguchi, Y., S. Nishino, and J. Inoue (2015), Fixed-point observation of mixed layer evolution in the seasonally ice-free Chukchi Sea: Turbulent mixing due to gale winds and internal gravity waves, *J. Phys. Oceanogr.*, in press, doi:10.1175/JPO-D-14-0149.1.

Kawano, T. (2010), Method for salinity (conductivity ratio) measurement, in *The GO-SHIP Repeat Hydrography Manual: A Collection of Expert Reports and Guidelines, IOCCP Rep. 14, ICPO Publ. Ser. 134*, edited by E. M. Hood, C. L. Sabine and B. M. Sloyan, UNESCO-IOC, Paris, France. [Available at www.go-ship.org/HydroMan.html.]

Kwok, R., G. F. Cunningham, M. Wensnahan, H. J. Zwally, and D. Yi (2009), Thinning and volume loss of the Arctic Ocean sea ice cover: 2003–2008, *J. Geophys. Res.*, *114*, C07005, doi:10.1029/2009JC005312.

Lee, S. H., T. E. Whitledge, and S.-H. Kang (2007), Recent carbon and nitrogen uptake rates of phytoplankton in Bering Strait and the Chukchi Sea, *Cont. Shelf Res.*, *27*, 2231–2249, doi:10.1016/j.csr.2007.05.009.

Lee, S. H., M. Jin, and T. E. Whitledge (2010), Comparison of bottom sea-ice algal characteristics from coastal and offshore regions in the Arctic Ocean, *Polar Biol.*, *33*, 1331–1337, doi:10.1007/s00300-010-0820-1.

Matsuno, T., J.-S. Lee, I.-C. Pang, and S.-H. Kim (2006), Monitoring the marine environment of the East China Sea with satellite-tracked drifters: Behavior of Changjiang diluted water [in Japanese with English abstract], *Bull. Coastal Oceanogr.*, *44*, 33–38.

McCabe, G. J., M. P. Clarc, and M. C. Serreze (2001), Trends in Northern Hemisphere surface cyclone frequency and intensity, *J. Clim.*, *14*, 2763–2768.

McLaughlin, F. A., and E. C. Carmack (2010), Deepening of the nutricline and chlorophyll maximum in the Canada Basin interior, 2003–2009, *Geophys. Res. Lett.*, *37*, L24602, doi:10.1029/2010GL045459.

Mordy, C. W., E. D. Cokelet, C. Ladd, F. A. Menzia, P. Proctor, P. J. Stabeno, and E. Wisegarver (2012), Net community production on the middle shelf of the eastern Bering Sea, *Deep Sea Res., Part II*, *65–70*, 110–125, doi:10.1016/j.dsr2.2012.02.012.

Niiler, P. P., A. S. Sybrandy, K. Bi, P. M. Poulain, and D. Bitterman (1995), Measurements of the water-following capability of holey-sock and TRISTAR drifters, *Deep Sea Res., Part I*, *42*(11/12), 1951–1964, doi:10.1016/0967-0637(95)00076-3.

Nishino, S. (2013), *R/V Mirai cruise report,* MR13-06, 226 p., JAMSTEC, Yokosuka, Japan. [Available at www.godac.jamstec.go.jp/darwin/datatree/e.].

Nishino, S., K. Shimada, and M. Itoh (2005), Use of ammonium and other nitrogen tracers to investigate the spreading of shelf waters in the western Arctic halocline, *J. Geophys. Res.*, *110*, C10005, doi:10.1029/2003JC002118.

Nishino, S., K. Shimada, M. Itoh, M. Yamamoto-Kawai, and S. Chiba (2008), East-west differences in water mass, nutrient, and chlorophyll *a* distributions in the sea-ice reduction region of the western Arctic Ocean, *J. Geophys. Res.*, *113*, C00A01, doi:10.1029/2007JC004666.

Nishino, S., K. Shimada, M. Itoh, and S. Chiba (2009), Vertical double silicate maxima in the sea-ice reduction region of the western Arctic Ocean: Implications for an enhanced biological pump due to sea-ice reduction, *J. Oceanogr.*, *65*, 871–883, doi:10.1007/s10872-009-0072-2.

Nishino, S., M. Itoh, W. J. Williams, and I. Semiletov (2013), Shoaling of the nutricline with an increase in near-freezing temperature water in the Makarov Basin, *J. Geophys. Res. Oceans*, *118*, 635–649, doi:10.1029/2012JC008234.

Orlanski, I. (1998), Poleward deflection of storm tracks, *J. Atmos. Sci.*, *55*, 2577–2602.

Poulsen, L. K., and N. Reuss (2002), The plankton community on Sukkertop and Fylla Banks off West Greenland during a spring bloom and post-bloom period: Hydrography, phytoplankton and protozooplankton, *Ophelia*, *56*(2), 69–85, doi:10.1080/00785236.2002.10409491.

Proshutinsky, A., R. Krishfield, M.-L. Timmermans, J. Toole, E. Carmack, F. McLaughlin, W. J. Williams, S. Zimmermann, M. Itoh, and K. Shimada (2009), Beaufort Gyre freshwater reservoir: State and variability from observations, *J. Geophys. Res.*, *114*, C00A10, doi:10.1029/2008JC005104.

Rainville, L., and R. A. Woodgate (2009), Observations of internal wave generation in the seasonally ice-free Arctic, *Geophys. Res. Lett.*, *36*, L23604, doi:10.1029/2009GL041291.

Rainville, L., C. M. Lee, and R. A. Woodgate (2011), Impact of wind-driven mixing in the Arctic Ocean, *Oceanography*, *24*, 136–145, doi:10.5670/oceanog.2011.65.

Sato, K., M. Aoyama, and S. Becker (2010), Reference materials for nutrients in seawater as calibration standard solution to keep comparability for several cruises in the world ocean in 2000s, in *Comparability of Nutrients in the World's Ocean*, edited by M. Aoyama et al., pp. 43–56, Mother Tank, Tsukuba, Japan.

Schlitzer, R. (2015), *Ocean Data View*, Alfred Wegener Institute, Bremerhaven, Germany. [Available at http://odv.awi.de.]

Sepp, M., and J. Jaagus (2011), Changes in the activity and tracks of Arctic cyclones, *Clim. Change*, *105*, 577–595, doi:10.1007/s10584-010-9893-7.

Serreze, M. C., J. E. Walsh, S. F. Chapin III, T. Osterkamp, M. Dyurgerov, V. Romanovsky, W. C. Oechel, J. Morison, T. Zhang, and R. G. Barry (2000), Observational evidence of recent change in the northern high-latitude environment, *Clim. Change*, *46*, 159–207.

Springer, A. M., and C. P. McRoy (1993), The paradox of pelagic food webs in the northern Bering Sea-III. Patterns of primary productivity, *Cont. Shelf Res.*, *13*, 575–599.

Stroeve, J., M. M. Holland, W. Meier, T. Scambos, and M. Serreze (2007), Arctic sea ice decline: Faster than forecast, *Geophys. Res. Lett.*, *34*, L09501, doi:10.1029/2007GL029703.

Tremblay, J.-É., and J. Gagnon (2009), The effects of irradiance and nutrient supply on the productivity of Arctic waters: A perspective on climate change, in *Influence of Climate Change on the Changing Arctic and Sub-Arctic Conditions*, edited by J. C. J. Nihoul and A. G. Kostianoy, pp. 73–92, Springer, Dordrecht, Netherlands.

Tremblay, J.-É., K. Simpson, J. Martin, L. Miller, Y. Gratton, D. Barber, and N. M. Price (2008), Vertical stability and the annual dynamics of nutrients and chlorophyll fluorescence in the coastal, southeast Beaufort Sea, *J. Geophys. Res.*, *113*, C07S90, doi:10.1029/2007JC004547.

Tsuchiya, K., T. Yoshiki, R. Nakajima, H. Miyaguchi, V. S. Kuwahara, S. Taguchi, T. Kikuchi, and T. Toda (2013), Typhoon-driven variations in primary production and phytoplankton assemblages in Sagami Bay, Japan: A case study of typhoon Mawar (T0511), *Plankton Benthos Res.*, *8*, 74–87.

Walsh, J. J., et al. (1989), Carbon and nitrogen cycling with the Bering/Chukchi Seas: Source regions for organic matter effecting AOU demands of the Arctic Ocean, *Prog. Oceanogr.*, *22*, 277–359.

Weingartner, T., K. Aagaard, R. Woodgate, S. Danielson, Y. Sasaki, and D. Cavalieri (2005), Circulation on the north central Chukchi Sea shelf, *Deep Sea Res., Part II*, *52*, 3150–3174, doi:10.1016/j.dsr2.2005.10.015.

Welschmeyer, N. A. (1994), Fluorometric analysis of chlorophyll *a* in the presence of chlorophyll *b* and pheopigments, *Limnol. Oceanogr.*, *39*, 1985–1992.

Wolk, F., H. Yamazaki, L. Seuront, and R. G. Lueck (2002), A new free-fall profiler for measuring biophysical microstructure, *J. Atmos. Oceanic Technol.*, *19*, 780–793.

Yamamoto-Kawai, M., N. Tanaka, and S. Pivovarov (2005), Freshwater and brine behaviors in the Arctic Ocean deduced from historical data of $\delta^{18}$O and alkalinity (1929–2002 A.D.), *J. Geophys. Res.*, *110*, C10003, doi:10.1029/2004JC002793.

Yang, J. (2009), Seasonal and interannual variability of downwelling in the Beaufort Sea, *J. Geophys. Res.*, *114*, C00A14, doi:10.1029/2008JC005084.

Yao, W., and R. H. Byrne (1998), Simplified seawater alkalinity analysis: Use of linear array spectrometers, *Deep Sea Res., Part I*, *45*, 1383–1392, doi:10.1016/S0967-0637(98)00018-1.

Zhang, J., C. Ashjian, R. Campbell, V. Hill, Y. H. Spitz, and M. Steele (2014), The great 2012 Arctic Ocean summer cyclone enhanced biological productivity on the shelves, *J. Geophys. Res. Oceans*, *119*, 297–312, doi:10.1002/2013JC009301.

Zhang, X., J. E. Walsh, J. Zhang, U. S. Bhatt, and M. Ikeda (2004), Climatology and interannual variability of Arctic cyclone activity: 1948–2002, *J. Clim.*, *17*, 2300–2317.